Numerical simulation of atmospheric-pressure 200 kHz / 13.56 MHz dual-frequency dielectric barrier discharges

Y. Liu[1,2], K. van 't Veer[1,2], F. J. J. Peeters[1], D. B. Mihailova[2], J. van Dijk[2], S. A. Starostin[3], M. C. M. van de Sanden[1,2] and H. W. de Vries[1,4]

[1]*Dutch Institute for Fundamental Energy Research, Eindhoven, 5612 AJ, The Netherlands*
[2]*Eindhoven University of Technology, Eindhoven, 5612 AZ, The Netherlands*
[3]*FUJIFILM Manufacturing Europe B.V., Tilburg, 5047 TK, The Netherlands*
[4]*FONTYS Hogescholen, Eindhoven, 5612 MA, The Netherlands*

Abstract: A one-dimensional drift-diffusion model is used to study atmospheric-pressure dual frequency (DF) dielectric barrier discharges in argon using the plasma modelling platform PLASIMO. The simulation exhibits an excellent agreement with the experimental results and gives insight into the DF plasma dynamics e.g. the electric field, the sheath edge profiles, the ionization/excitation rate and the electron energy distribution function (EEDF) profiles. The results indicate that due to the RF oscillation, the electric field, the sheath edge and thus the ionization/excitation are temporally modulated. As a result, the plasma conductivity is enhanced as the plasma density is higher. The discharge development is slowed down with a lower current amplitude and a longer duration. The time-averaged sheath is getting thinner with a more pronounced ionization rate and a longer contacting time near the substrate, which could help to improve the efficiency of plasma-assisted surface processing. In addition, the DF excitation exhibits a capability of modifying the EEDF profiles and controlling the plasma chemical kinetics, which can be applied to the other relevant fields e.g. gas phase chemical conversion.

1. Introduction

Atmospheric-pressure (AP) large area diffuse plasma is highly required in various applications including plasma-assisted gas phase chemical conversion, surface modification and synthesis of high quality functional thin films [1–4]. One of the common ways to create a large area non-thermal plasma at atmospheric pressure is the dielectric barrier discharge (DBD) [1,2,4]. Compared to the other sources of atmospheric-pressure plasma [5,6] e.g. corona discharge and atmospheric-pressure plasma jet (APPJ), the DBD is characterized by low gas consumption, a considerably high specific power density and strong potential for up scaling [7]. However, an atmospheric-pressure DBD is typically filamentary. The less common diffuse modes of DBD are usually limited by the use of gas mixtures, frequency, input power and so on. In recent years, AP-DBD has been widely investigated in various gas mixtures [8–11] with both experimental [12–14] and numerical simulation [15–20] methods. In addition, in our previous research, a high-current diffuse DBD in atmospheric-pressure low cost $N_2/O_2/Ar$ gas mixtures has been obtained [7,21–23]. Using this discharge as the plasma source, high quality silica-like barrier layers with a uniform surface, a low level of defects and thus an excellent permeation property have been deposited on polymeric substrates [21,24,25].

In order to improve efficiency of plasma processing, a dual frequency (DF) excitation system was introduced by applying an extra radio frequency (RF) voltage at 13.56 MHz on the low frequency (LF) voltage at 200 kHz [26,27]. This dual frequency (DF) excitation was previously investigated in low-pressure plasmas [28–34] as well as atmospheric-pressure plasmas [35–41]. Under atmospheric pressure, the effects of the DF excitation are focused on tailoring the electron energy distribution function (EEDF) and controlling the plasma parameters e.g. electron density, gas temperature and ion flux to the sample [35,37–39]. The high frequency voltage allows to trap the electrons in the plasma bulk with less electron loss at the surface and leads to a higher power coupled into electrons [38,42]. This helps to maintain a high plasma density and enhance the elastic collision and thus the gas temperature [38,40,41]. The low frequency voltage extracts the ions from bulk region to the cathode sheath and leads to the synthesis of a denser film with an improved microstructure compared to the pure RF DBD excitation [36,43]. Additionally, in our

work, it was found that due to the periodic oscillation of the RF electric field, the electron heating and thus the gas ionization is temporally modulated, leading to a slower discharge development and thus an improved uniformity of AP-DBD [44]. Furthermore, by tuning the amplitude ratio of the superimposed LF and RF signals, the DF excitation also exhibits capability of modifying the electron energy distribution function (EEDF), which can be applied to the other fields e.g. plasma-assisted gas phase chemical conversion [45].

In this study, a time-dependent, one-dimensional drift-diffusion model was employed to study the electrical characteristics of atmospheric-pressure DF dielectric barrier discharges. The paper is organised as follows: the methods including experimental and simulation are introduced in section. 2. The results including the electrical characteristics and the phase-resolved DF plasma dynamics are presented in section.3. The conclusions and outlook are given in section. 4.

2. Methods

2.1. Experimental

The detailed description of the experimental setup for the atmospheric-pressure DF discharge has been given elsewhere [44,45]. Here only the main parameters of the system are briefly introduced. The discharge was ignited between a flat bottom electrode and a curved top electrode with a radius of 60 mm and a width of 45 mm. Both the electrodes were covered by 0.1 mm thick PET (polyethyleneterephtalate) foils as the dielectrics. The electrode temperature was maintained at 30 ℃ by means of an oil circulation system. The smallest distance between the two electrodes was 1.0 mm. The gas (99.99% Ar) was injected into the discharge area with a flow rate at 10 slm (standard litre per minute). The substrates were transported at 40 mm/min. The top electrode was excited by 200 kHz LF (SEREN L3001) and 13.56 MHz RF (SEREN R601) power sources, while the bottom electrode was grounded. The injected power of both power sources was modulated at 625 Hz with a pulse width of 800 µs and a duty cycle of 50%. An intensified charge-coupled device (ICCD) camera (PI MAX3), triggered by the applied voltage, was employed to collect the discharge emission from the side view of the gas gap with a macro lens (Tamron AF 90 mm).

2.2. Simulation

2.2.1. Model equations

To gain a better understanding of the physical and chemical processes in the plasma, a time-dependent one-dimensional drift-diffusion model with the plasma platform PLASIMO was employed [46]. Details about PLASIMO can be found in Ref. [47,48]. The MD2D code is dedicated to the construction of Grand models for plasmas in which the gas heating and gas flow are less or not important.

The model is based on the balance equations derived from the Boltzmann equation [49]:

$$\frac{\partial f_p}{\partial t} + \mathbf{v} \cdot \nabla_{\mathbf{x}} f_p + \mathbf{a} \cdot \nabla_{\mathbf{v}} f_p = \left(\frac{\partial f_p}{\partial t}\right)_{cr} \tag{1}$$

in which f_p ($\mathbf{x}$, $\mathbf{v}$, t) is the distribution function of species p, $\mathbf{x}$ and $\mathbf{v}$ the position and velocity, respectively. $\mathbf{a}$ is the acceleration of the particles under the influence of external forces. The gradients $\nabla_{\mathbf{x}}$ and $\nabla_{\mathbf{v}}$ are the derivatives with respect to the position and velocity components, respectively. The subscript *cr* denotes the influence of collisions and radiation.

The first three moments of the Boltzmann equation are obtained by multiplying it by m_p, $m_p\mathbf{v}$ and $1/2 m_p v^2$, respectively, and integrating the result over the velocity space. This gives the balance equations of particle, momentum and energy conservation.

The zeroth moment of the Boltzmann equation leads to the particle balance equation:

$$\frac{\partial n_p}{\partial t} + \nabla \cdot \mathbf{\Gamma}_p = S_p, \tag{2}$$

where n_p is the density, $\mathbf{\Gamma}_p$ the flux density and S_p the source term (due to reactions) of species p.

The first moment of the Boltzmann equation leads to the momentum balance equation, from which can be derived the drift-diffusion flux:

$$\mathbf{\Gamma}_p = \mu_p \mathbf{E} n_p - D_p \nabla n_p, \tag{3}$$

where μ_p is the mobility, D_p the diffusion coefficient of species p and $\mathbf{E}$ the electric field. In the derivation, viscosity and inertia are neglected and an ideal gas, acceleration due to the electric field only, small collision times and dominance of the background gas are assumed [49,50].

The second moment leads to the energy balance equation:

$$\frac{\partial n_\varepsilon}{\partial t} + \nabla \cdot \mathbf{\Gamma}_\varepsilon = S_\varepsilon, \tag{4}$$

with $\mathbf{\Gamma}_\varepsilon$ the electron energy flux:

$$\mathbf{\Gamma}_\varepsilon = \frac{5}{3} \mu_e \mathbf{E} n_\varepsilon - \frac{5}{3} D_e \nabla n_\varepsilon, \tag{5}$$

where $n_\varepsilon = n_e \varepsilon$ is the mean electron energy density and μ_e the mobility of electrons. In this derivation proportionality of the heat flux with the energy gradient and a Maxwellian distribution is assumed [50].

The source term S_p in equation (2) is obtained by considering the volume reactions in which particles are created or lost:

$$S_p = \sum_r c_{r,p} R_r = \sum_r \left[c_{r,p} k_r \prod_q n_q \right] \tag{6}$$

where $c_{r,p}$ is the stoichiometric number of species p in reaction r, and R_r the reaction rate. The reaction rate is a product of reaction coefficient k_r and densities of the reacting species n_q.

The electron energy source term S_ε in equation (4) is:

$$S_\varepsilon = \mathbf{\Gamma}_e \cdot \mathbf{E} - \sum_r \varepsilon_r R_r - L_\varepsilon, \tag{7}$$

in which the first term is due to the heating by the electric field, the second represents the energy loss in inelastic collisions, and the last term L_ε represents the energy loss due to elastic collisions with the heavy components.

The transport equations — the particle balance equation (2), the momentum balance equation (3) and the energy balance equation (4) — are coupled to the Poisson equation for the computation of the electric field:

$$\nabla \cdot (\epsilon \mathbf{E}) = -\nabla \cdot (\epsilon \nabla V) = \rho = \sum_p q_p n_p \tag{8}$$

3

where ϵ is the dielectric permittivity, V the electrostatic potential, ρ the space charge density and q_p the charge of the species p.

The boundary conditions on material surfaces for the particle transport equations in this study are described as follows:

$$\mathbf{\Gamma}_p \cdot \hat{\mathbf{n}} = n_p \left(\alpha_p \mu_p \mathbf{E} \cdot \hat{\mathbf{n}} + \tfrac{1}{4} v_{th,p} \right), \tag{9}$$

where $\hat{\mathbf{n}}$ is the normal vector pointing toward the surface, α_p the switching function defined as:

$$\alpha_p = \begin{cases} 1, & \mu_p \mathbf{E} \cdot \hat{\mathbf{n}} > 0, \\ 0, & \mu_p \mathbf{E} \cdot \hat{\mathbf{n}} \leq 0. \end{cases} \tag{10}$$

$v_{th,p}$ is the thermal velocity of the species and is given by

$$v_{th,p} = \sqrt{\frac{8 k_B T_p}{\pi m_p}}, \tag{11}$$

where k_B is the Boltzmann constant, m_p the mass and T_p the temperature of species p.

For the electrons the situation is more complicated since, in addition to the terms in equation (9), the flux $\mathbf{\Gamma}_\gamma$ due to secondary emission also needs to be taken into account:

$$\mathbf{\Gamma}_e \cdot \hat{\mathbf{n}} = n_e \left(\alpha_e \mu_e \mathbf{E} \cdot \hat{\mathbf{n}} + \frac{1}{4} v_{th,e} \right) - \sum_p \gamma_p \, \mathbf{\Gamma}_p \cdot \hat{\mathbf{n}} \tag{12}$$

where γ_p is the secondary electron emission coefficient.

The boundary conditions for the mean electron energy density is analogous

$$\mathbf{\Gamma}_\varepsilon \cdot \hat{\mathbf{n}} = n_\varepsilon \left(\alpha_e \frac{5}{3} \mu_e \mathbf{E} \cdot \hat{\mathbf{n}} + \frac{1}{3} v_{th,e} \right) - \sum_p \gamma_p \, \varepsilon_{\gamma,p} \mathbf{\Gamma}_p \cdot \hat{\mathbf{n}} \tag{13}$$

where $\varepsilon_{\gamma,p}$ is the initial mean energy of emitted electrons.

For the Poisson equation (8), the boundary condition on a dielectric-plasma interface is:

$$\epsilon_{diel} \mathbf{E}_{diel} \cdot \hat{\mathbf{n}} - \epsilon_0 \mathbf{E}_{gas} \cdot \hat{\mathbf{n}} = \sigma, \tag{14}$$

$$\sigma = \int \mathbf{j} \cdot \hat{\mathbf{n}} \, dt, \tag{15}$$

$$\mathbf{j} = \sum_p q_p \mathbf{\Gamma}_p, \tag{16}$$

4

where ϵ is the permittivity, σ is the surface charge density which is assumed static after deposition and **j** the current density. Other relevant boundaries are open boundaries, where the boundary conditions for the densities and potential are Homogeneous Neumann.

2.2.2. Species and reactions

In this study, four species (i.e. electrons, Ar^+, Ar_2^+ and Ar metastables) are considered in the description of the argon chemistry. Table. 1 lists those species and the related (transport coefficients) input. The ion mobility is experimentally determined as function of the reduced electric field [51]. The diffusion coefficient for Ar^* is calculated using a collision integral method [52], which is evaluated at the gas temperature. The electron mobility is calculated as a function of the mean electron energy from the EEDF using Boltzmann solver BOLSIG+ [53], from which the chemical reaction rate coefficients involving electrons are also obtained.

Table 1. The species and their transport coefficients used in the model.

Species	ε_{th} (eV)	$\mu_p N$	$D_p N \left(\mathrm{m^{-1} s^{-1}} \right)$	Ref.
e	0	$\mu_e N(\varepsilon)$	Einstein	[54]
Ar^*	11.55	no charge	$6.45163 \cdot 10^{20}$	[52]
Ar^+	15.759	$\mu_{Ar^+} N(E/N)$	Einstein	[51]
Ar_2^+	14.5	$\mu_{Ar_2^+} N(E/N)$	Einstein	[51], [55]

The total used set of reactions and the rate coefficients are given in Table. 2. This includes excitation (R1) and de-excitation (R2), stepwise (R3) and direct ionization (R4), metastable-metastable ionization – both regular (R5) and associative (R6), atomic to molecular (R7) and molecular to atomic (R8) ion conversions, dissociative recombination (R9), three-body recombination (R10, 11) and radiative decay (R12).

2.2.3. setup and conditions

Unlike the practical setup with a non-uniform electrode configuration [44,45], in the simulation a conventional DBD system with two parallel electrodes is used. Both the electrodes are covered by an insulating layer with a dielectric constant of 3.4. The discharge is generated in an effective discharge area of 1 m × 1 m with a narrow gas gap of 1.0 mm. One electrode is grounded, while the other one is driven by a DF voltage composed of 200 kHz LF and 13.56 MHz RF waveforms. The gas temperature is fixed at $T_g = 450$ K [60]. The secondary electron emission coefficient (γ) is set to 0.07 [61]. Reflection coefficients are not considered in this study [58]. The LF voltage (U_{LF}) is maintained at 1000 V, while the RF voltage (U_{RF}) gradually increases from 0 V to 250 V.

Table 2. The reactions and their rate coefficients as are taken into account in the drift-diffusion model.

Index	Reaction	Rate coefficient	Ref.
1	$e + Ar \rightarrow Ar^* + e$	$k_1(\varepsilon)$	[54]
2	$e + Ar^* \rightarrow Ar + e$	$k_2(\varepsilon)$	[54]
3	$e + Ar^* \rightarrow Ar^+ + e + e$	$k_3(\varepsilon)$	[54]
4	$e + Ar \rightarrow Ar^+ + e + e$	$k_4(\varepsilon)$	[54]
5	$Ar^* + Ar^* \rightarrow Ar^+ + e + Ar$	$5.16 \cdot 10^{-16} \text{ m}^3\text{s}^{-1}$	[56,57]
6	$Ar^* + Ar^* \rightarrow Ar_2^+ + e$	$4.64 \cdot 10^{-16} \text{ m}^3\text{s}^{-1}$	[56,57]
7	$Ar^+ + Ar + Ar \rightarrow Ar_2^+ + Ar$	$2.5 \cdot 10^{-43}(300/T[K])^{3/2} \text{ m}^6\text{s}^{-1}$	[58]
8	$Ar_2^+ + Ar \rightarrow Ar^+ + Ar + Ar$	$5.22 \cdot 10^{-16}T[eV]^{-1} \exp(-1.304/T[eV]) \text{ m}^3\text{s}^{-1}$	[58]
9	$e + Ar_2^+ \rightarrow Ar^* + Ar$	$7 \cdot 10^{-13} \cdot (300/T_e[K])^{1/2} \text{ m}^3\text{s}^{-1}$	[58]
10	$e + Ar^+ + e \rightarrow Ar + e$	$8.75 \cdot 10^{-39}T_e[eV]^{-9/2} \text{ m}^6\text{s}^{-1}$	[58]
11	$e + Ar^+ + Ar \rightarrow Ar + Ar$	$1.5 \cdot 10^{-40}(300/T[K])^{2.5} \text{ m}^6\text{s}^{-1}$	[59]
12	$Ar^* \rightarrow Ar + h\nu$	$6.24 \cdot 10^5 \text{ s}^{-1}$	[55]

3. Results and discussions

3.1. Electrical characteristics

3.1.1. Voltage-current waveforms

The simulated voltage and current density waveforms of the DF discharges within one LF cycle (5 µs) are illustrated in Figure 1. The LF discharge current contains a single smooth peak every half LF cycle, while in the DF discharges ($U_{RF} > 0$ V), both the current density and the voltage are a superposition of the LF and RF components. By doing fast Fourier transform (FFT) of the original waveforms, the fundamental signals of LF (200 kHz) and RF (13.56 MHz) in the DF discharge can be separated in the frequency domain. Typical FFT spectra of voltage and current density in the DF discharge ($U_{LF} = 1000$ V, $U_{RF} = 250$ V) are shown in Figure 2. The FFT amplitudes of current density as a function of U_{RF} are presented in Figure 3. With U_{RF} increasing from 0 V to 250 V, the LF current density increases slightly from 17.3 A to 19.2 A, while the RF current density increases significantly from 0 A to 60.9 A. A similar electrical behaviour was also observed in the experimental study in Ref. [44], which is attributed to the fast increase of the capacitive component of the RF current [62].
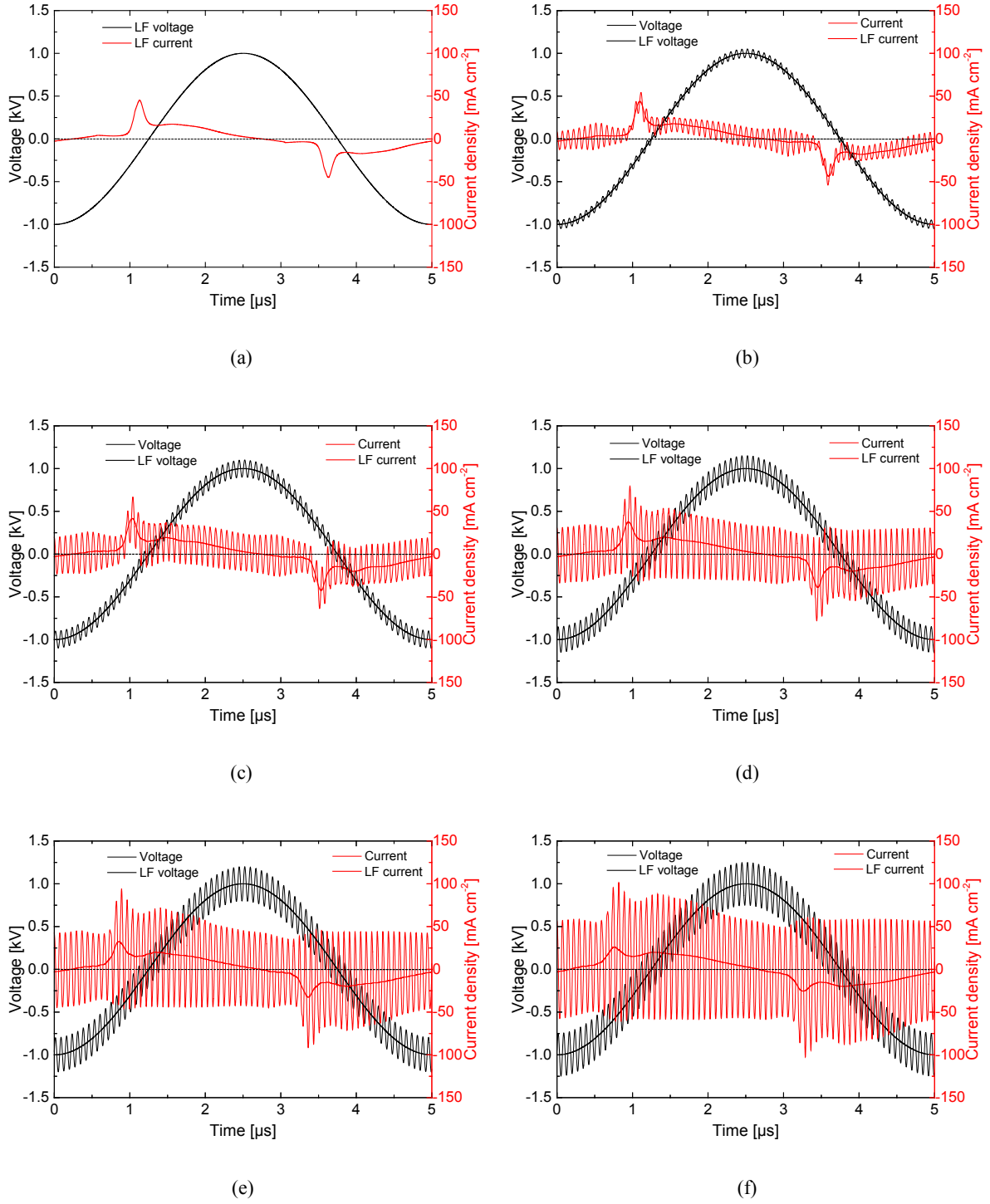
Figure. 1. Original and FFT-filtered voltage-current density waveforms of the DF discharges with U_{RF} of (a) 0 V, (b) 50 V, (c) 100V, (d) 150 V, (e) 200 V and (f) 250 V. U_{LF} = 1000 V under all conditions.
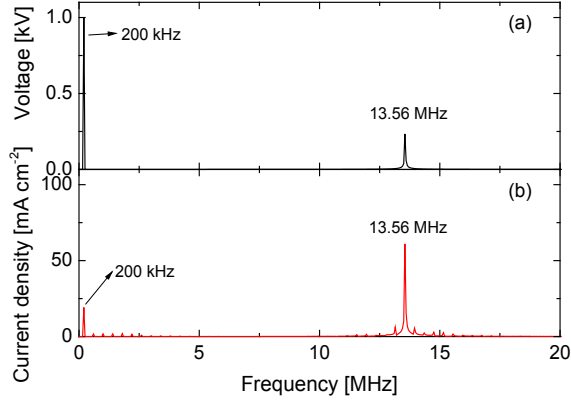
Figure. 2. Fast Fourier transform (FFT) spectra of (a) voltage and (b) current density in the DF discharge with $U_{LF} = 1000$ V, $U_{RF} = 250$ V.
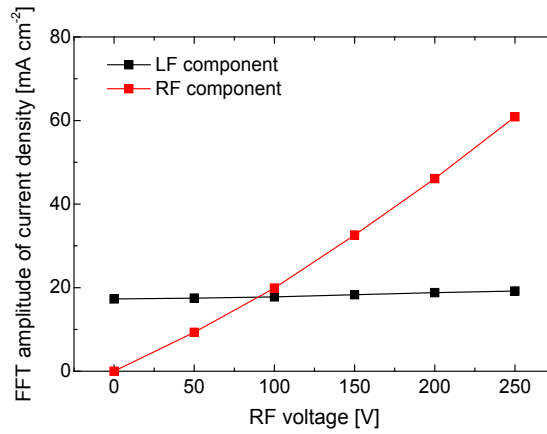

Figure. 3. Variations of the FFT current density components as a function of U_{RF}.

3.1.2. Lissajous figures

The charge-voltage characteristics (often referred as Lissajous figures) can be used for the determination of discharge power, charge transferred through the gas gap and effective dielectric capacitance [13,63,64]. In this work, by doing fast Fourier transfer (FFT) filtering of the original Lissajous figures, signals above 10 MHz (including 13.56 MHz RF oscillation) are removed, and the LF component can be extracted. The FFT-filtered, LF-induced Lissajous figures are reconstructed and presented in Figure. 4. Unlike the classical electrical theory that Lissajous figures have a form of parallelogram and can be divided into "plasma-off" and "plasma-on" phases [1,13,65,66], under these conditions, the FFT-filtered Lissajous figures have an irregular shape. Therefore, three phases are introduced: Lines AB and DE represent the phases when no plasma is ignited, lines BC and EF represent the phases when the plasma is fast developing, and lines CD and FA represent the phases of plasma decay, see Figure. 4. The slope during each phase represents the corresponding equivalent capacitance [66], which are presented in Figure. 5 as a function of U_{RF}. With U_{RF} increasing, the "plasma-off" periods (AB and DE) are getting shorter, and the equivalent capacitance increases. Both the "plasma-developing" periods (BC and EF) and the "plasma-decay" periods (CD and FA) become longer. The capacitance of the "plasma-developing" periods (BC and EF) decreases, while the capacitance of the "plasma-decay" periods (CD and FA) is relatively constant.
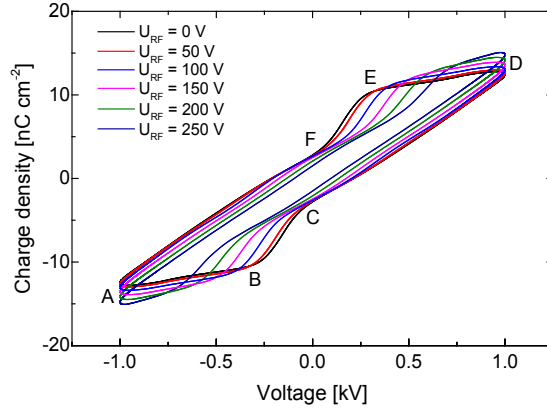
8

Figure. 4. FFT-filtered Lissajous figures of the DF discharges with various RF voltage amplitudes.
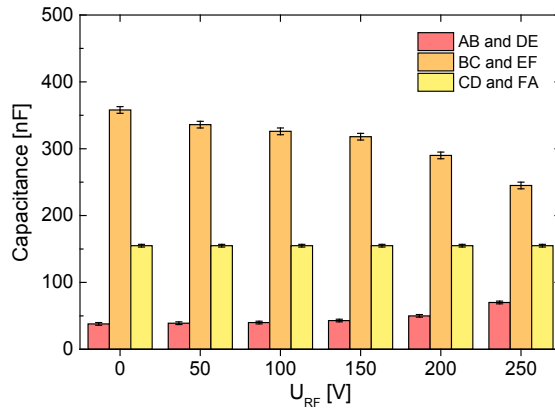

Figure. 5. Variations of the capacitances during different phases as a function of U_{RF}. The letters A-F correspond to those in Figure. 4.

3.1.3. Gas voltage and discharge current

From the applied voltage and current in section. 3.1.1 and the equivalent capacitances in section. 3.1.2, the gas gap voltage (U_{gas}) and discharge current ($I_{discharge}$) can be further obtained [13,63,67]. The FFT-filtered, LF induced gas voltage, discharge current and plasma conductivity of the DF discharges during the positive LF half cycle (2.5 µs) are presented in Figure. 6. The breakdown voltage, the maximal LF discharge current, the input power and the maximal plasma conductivity as a function of U_{RF} are presented in Figure. 7, which exhibit a good agreement with the experimental results in Ref. [44].

From Figure. 6(a), the LF gas voltage experiences a considerable decrease after the gas breakdown under all conditions, which is induced by the formation of a cathode fall [62]. With an increased U_{RF}, the total LF gas voltage gradually decreases, which is mainly induced by the enhancement of the charge transferred to the dielectric surface and thus the higher voltage applied to the dielectrics. Since the total LF voltage is constant ($U_{LF} = 1000$ V), the LF gas voltage is therefore reduced.

From Figure. 6(b), the discharge currents contain a main peak and a tail after that. The total breakdown voltage is relatively constant under these conditions (~ 80 V). With an increased U_{RF}, the plasma ignition moment within the

LF cycle is therefore brought forward. Moreover, a lower amplitude and a longer discharge duration of the LF discharge current can be observed, indicating a slower discharge development and thus a more uniform and stable plasma [44,68].

From Figure. 6(c), the plasma conductivity σ_{plasma} is zero before the breakdown, fast increases during the "plasma-developing" period, and gradually declines during the "plasma-decay" period. With an increased U_{RF}, the amplitude of σ_{plasma} is gradually enhanced during both "plasma-developing" and "plasma-decay" periods due to the higher plasma density.

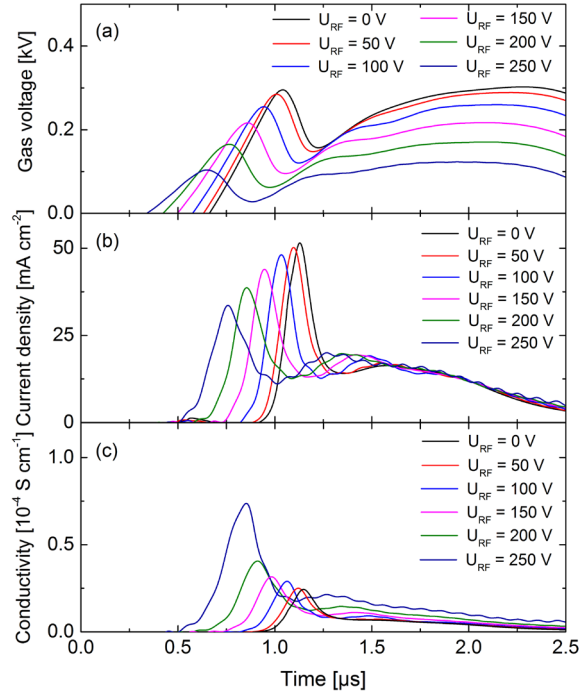Figure. 6. FFT-filtered (a) gas voltage, (b) discharge current density and (c) plasma conductivity of the DF discharges with U_{LF} = 1000 V and U_{RF} = 0-250 V.
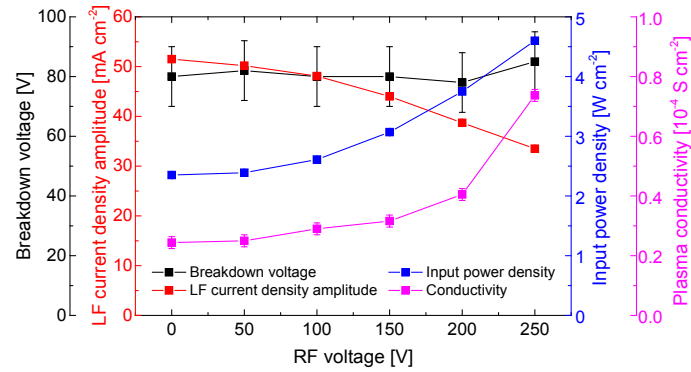

Figure. 7. Variations of the breakdown voltage, the maximal LF current amplitude, the input power density and the maximal plasma conductivity as a function of U_{RF}. U_{LF} = 1000 V under all conditions.

10

3.1.4. Equivalent DF electrical circuit

An equivalent circuit model of a DBD discharge was previously introduced [13,65] and can be used to infer discharge properties from measured voltage $V(t)$ and current $I(t)$ waveforms, as presented in Figure. 8(a). The plasma is assumed to be a parallel connection of a variable resistor $R_{LF}(t)$ and a gas gap capacitor C_{gas}, which is then in series with the dielectric capacitance C_{diel}. To distinguish between geometrically determined dielectric capacitance C_{diel} and the equivalent dielectric capacitance defined from the slopes (dQ/dV) in the Lissajous figures, the latter is referred to as ζ_{diel}. During the "plasma-off" phases (AB and DE in Figure. 4), $R_{LF}(t)$ has an infinite resistance and there is no charge transfer through the gas gap. The reactor capacitance is equal to $C_{cell} = \frac{C_{diel} \cdot C_{gas}}{C_{diel} + C_{gas}}$ ($\sim$ 38 nF in this study). During the "plasma-developing" phase (BC and EF), due to the fast increasing plasma density, the resistance of $R_{LF}(t)$ is rather low (Figure. 6(c)). A large amount of charge is transferred through the gas gap within a short time, leading to an overrated capacitance of the dielectrics ζ_{diel} ($\sim$ 358 nF). During the "plasma-decay" period (CD and FA), the resistance of $R_{LF}(t)$ and thus the plasma conductivity is relatively constant. The charge keeps being delivered through the gas gap. The estimated equivalent capacitance ζ_{diel} ($\sim$ 155 nF) is approximately equal to C_{diel} (150 nF), see Figure. 5.

For the DF discharges, due to the extra RF electric field, the DF equivalent electrical circuit should be modified with an extra variable resistor $R_{RF}(t)$ and an equivalent capacitor $\zeta_{RF}(t)$ [45], see Figure. 8(b). During the "plasma-off" phase (AB and DE in Figure. 4), the gas gap is not completely free of charge. Instead, a certain amount of charge is trapped in the gas gap by the RF electric field. The temporally-oscillating RF electric field therefore works as an equivalent capacitance (see Ref. [8] for more detailed information). As a result, $\zeta_{gas}(t) = C_{gas} + \zeta_{RF}(t)$ is higher than C_{gas}, thus $\zeta_{cell}(t) = \frac{C_{diel} \cdot \zeta_{gas}(t)}{C_{diel} + \zeta_{gas}(t)} = \frac{C_{diel} \cdot (C_{gas} + \zeta_{RF}(t))}{C_{diel} + (C_{gas} + \zeta_{RF}(t))}$ is higher than $C_{cell} = \frac{C_{diel} \cdot C_{gas}}{C_{diel} + C_{gas}}$ ($\sim$ 38 nF). With a higher U_{RF}, the RF electric field is enhanced, and more charge can be trapped in the gas gap. Thus the equivalent capacitance $\zeta_{RF}(t)$ is higher, leading to the increase of $\zeta_{gas}(t)$ and thus $\zeta_{cell}(t)$, see Figure. 4 and 5. During the "plasma-developing" phase (BC and EF), due to the RF oscillation, the discharge development is slowed down with a lower amplitude and a longer duration [44], see Figure. 6(b). The process of charge transfer through the gas gap therefore is slower. As a result, the estimated equivalent capacitance ζ_{diel} decreases with U_{RF}, which however is still higher than C_{diel} ($\sim$ 150 nF). During the "plasma-decay" phase (CD and FA), the plasma conductivity is relatively constant (Figure. 6(c)). The RF electric field works as an extra conductor $R_{RF}(t)$ in parallel to $R_{LF}(t)$. The equivalent resistance of plasma $R_{gas}(t) = \frac{R_{LF}(t) \cdot R_{RF}(t)}{R_{LF}(t) + R_{RF}(t)}$ is lower than $R_{LF}(t)$. The equivalent capacitance ζ_{diel} however is not influenced by U_{RF} and is constant ($\sim C_{diel}$), see Figure. 4 and Figure. 5.
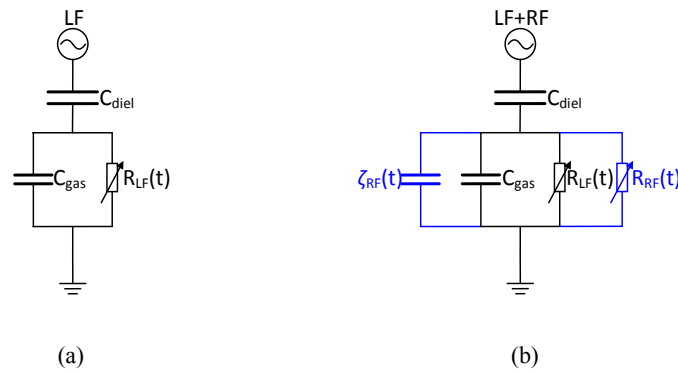

Figure. 8. Equivalent electrical circuits of (a) LF discharge and (b) DF discharge.

3.2. Phase resolved plasma dynamics

3.2.1. LF vs DF

Figure. 9 shows the plasma parameters of LF and DF discharges within one LF cycle (5 µs). The phase and space resolved electric field, power absorbed by electrons, direct ionization rate, excitation rate and experimental discharge emission are presented in plots (a) to (j). The solid lines indicate the sheath edges between the plasma bulk and the plasma sheath, which are determined assuming an equivalent sharp electron step [69]. The method to obtain the phase resolved discharge emission was previously introduced in [26,27,70].
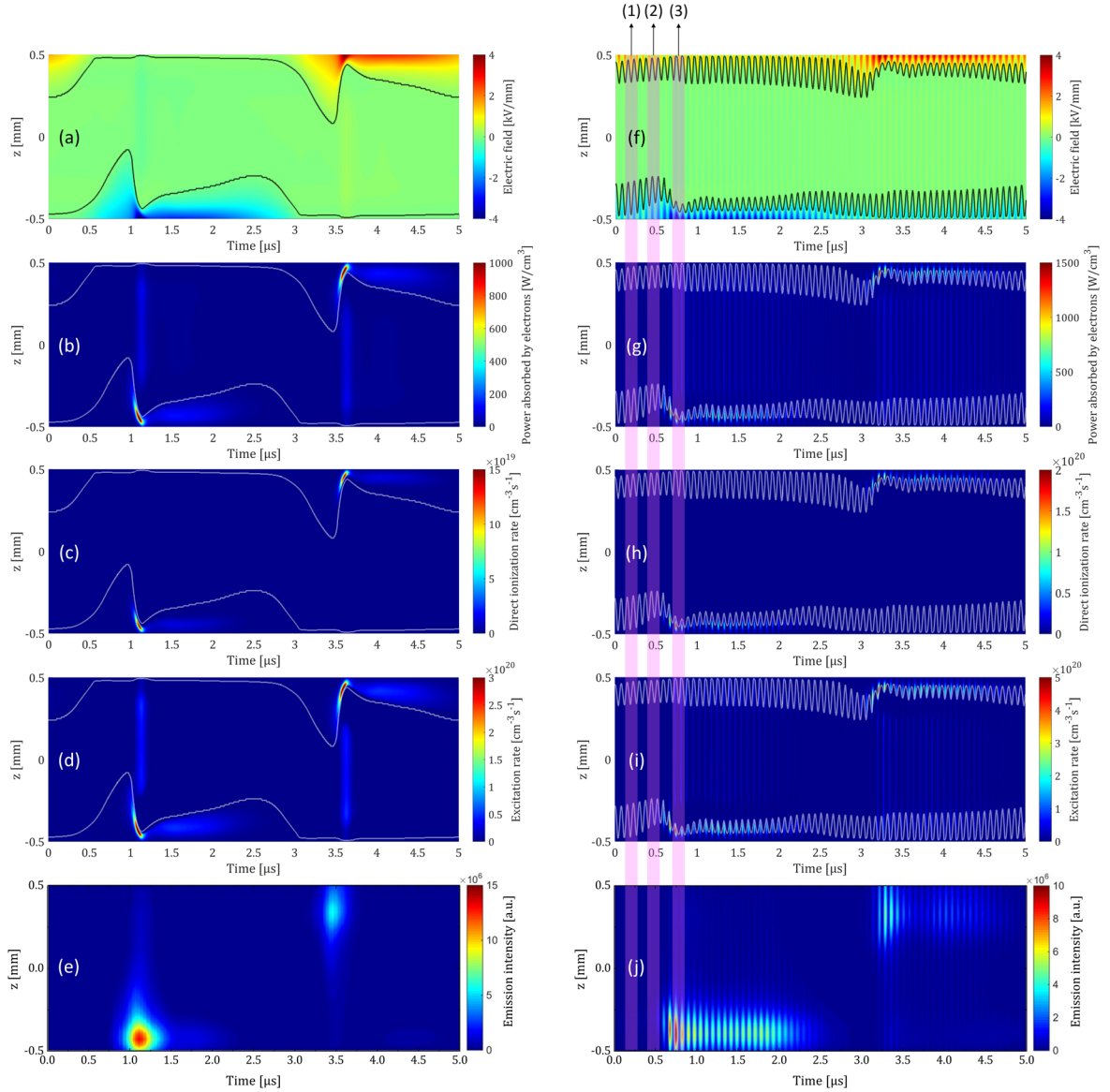

Figure. 9. Phase and space resolved electric field (first row), power absorbed by electrons (second row), direct ionization rate (third row), excitation rate (fourth row) and experimental discharge emission (fifth row). Left column: LF discharge with U_{LF} = 1000 V, right column: DF discharge with U_{LF} = 1000 V and U_{RF} = 250 V. The solid lines indicate the sheath edges. The shaded areas in the right column indicate the 3 phases which would be discussed in the following section.

A good agreement between the experimental discharge emission (Figure. 9(e) and (j)) and the simulated excitation rate profiles (Figure. 9(d) and (i)) is found in both LF and DF discharges. The asymmetrical structure of the discharge emissions between two opposite polarities of the voltage is attributed to the particular electrode configuration (a top curved electrode and a bottom flat electrode) in this study [44,45]. The ionization rate (Figure. 9(c) and (h)) is a few times lower than the excitation rate (Figure. 9(d) and (i)) and can only be observed inside the sheath. This is due to the higher ionization threshold (15.8 eV) than the excitation threshold (11.5 eV). The high energy electrons are mainly generated in the strong electric field (maximum 4 kV/mm) inside the sheath (Figure. 9(a) and (f)), while the dominant electron power absorbance in the bulk area is through Ohmic heating [71]. In this study, the electron power absorbance (Figure. 9(b) and (g)) has the same spatio-temporal pattern as the excitation rate (Figure. 9(d) and (i)).

The variations of the average excitation and ionization rates as a function of U_{RF} are presented in Figure. 10. With U_{RF} increasing from 0 V to 250 V, the ionization rate slightly increases from 5.35×10^{17} cm^{-3} s^{-1} to 6.55×10^{17} cm^{-3} s^{-1}, while the excitation rate increases more significantly from 3.70×10^{18} cm^{-3} s^{-1} to 6.44×10^{18} cm^{-3} s^{-1}. To investigate the ionization/excitation mechanisms, the time and space averaged, density weighted electron energy distribution functions (EEDFs) [72] of the DF discharges as a function of U_{RF} are obtained †, as shown in Figure. 11. It can be seen that the high energy tail of the EEDFs above 13.5 eV is not obviously influenced, while the energy range below 13.5 eV exhibits a significant enhancement with U_{RF}. Since the ionization threshold of Ar (15.8 eV) is much higher than the excitation threshold (11.5 eV), the excitation rate therefore experiences a more pronounced enhancement than the ionization rate with U_{RF} increasing, as presented in Figure. 10.
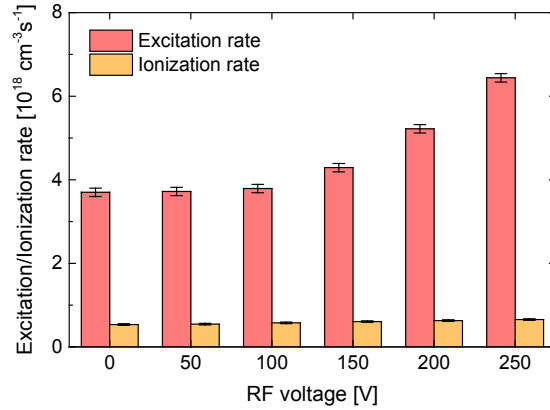

Figure. 10. Spatially integrated excitation/ionization rate within one LF cycle (5 μs) as a function of U_{RF}.

† From BOLSIG+, EEDFs $f_{E/N}(\varepsilon)$ are calculated at various static reduced electric fields E/N. Here ε is the electron energy itself. To each EEDF a mean electron energy $\bar{\varepsilon}$ is assigned. The drift-diffusion model yields $\bar{\varepsilon}(\mathbf{x}, t)$ such that an EEDF $f(\mathbf{x}, t, \varepsilon)$ can be assigned. The reported averaged EEDFs $\bar{f}(\varepsilon)$ are: $\bar{f}(\varepsilon) = \langle n_e(\mathbf{x}, t) f(\mathbf{x}, t, \varepsilon) \rangle_{\mathbf{x}, t}$.
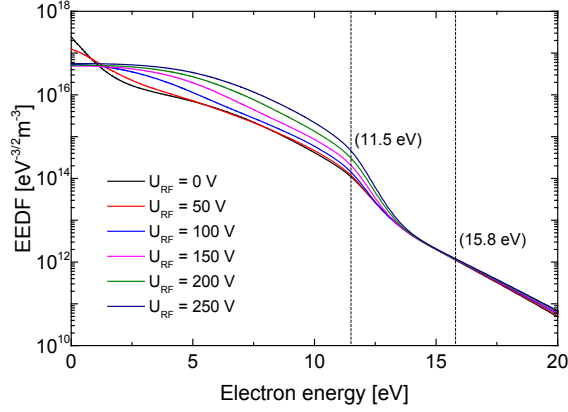
Figure. 11. Electron energy distribution function (EEDF) of the DF discharges as a function of U_{RF}.

To further investigate the plasma dynamics, the sheath edge profiles near the cathode during half a LF cycle (2.5 μs) of the LF and DF discharges are presented in Figure. 12. For the single LF discharge ($U_{LF} = 0$ V), before the gas breakdown the sheath edge is close to the bottom electrode (~ 30 μm), where the ion density is relatively low. With the gas voltage increasing, the sheath is getting thicker together with a higher electric field within the sheath. The maximal LF sheath thickness under these conditions is ~ 420 μm. The electrons are generated through secondary electron emission (γ process) from the cathode by ion bombardment and accelerated by the electric field within the sheath. As the gas voltage further increases, the gas breakdown occurs, leading to a fast increase of ion density inside the sheath. The ionization rate under these conditions is high enough to create a density of ions able to localize the electric field. The formation of the cathode fall enhances the ionization close to the cathode [62] and reduces the sheath thickness. When the ionization rate is maximum, the sheath thickness is minimum (~ 60 μm). During the discharge decay, the ionization rate and thus the ion density decreases inside the sheath. The sheath therefore is gradually getting thicker, as shown in Figure. 12(a).

For the DF discharge, due to the RF oscillation, the sheath edge is periodically modulated, see Figure. 12(a). Before the breakdown, the LF-induced sheath is thicker (Figure. 12(b)), the averaged electron energy within the sheath therefore is enhanced, causing a higher possible ionization rate. Since the local ion density is relatively low, and the plasma sheath oscillation is rather violent for a given RF voltage change [31] (Figure. 12(c)). The maximal LF sheath thickness is ~ 185 μm — much less than the LF discharge (~ 420 μm). After the breakdown, the ions generated inside the sheath induce a cathode fall near the electrode and lead to a reduced LF sheath thickness. The minimum LF sheath thickness (~ 60 μm) is the same as the LF discharge, while the RF sheath oscillation amplitude is minimum due to the maximal local ion density at this moment. During the decay, the LF sheath thickness is gradually getting thicker but still lower than the LF discharge, which is supposed to be related to the higher ionization rate and thus the higher ion density inside the sheath.

It is known that the chemistry and thus the concentrations of reactive species in the sheath, is the key point in plasma-assisted thin film processing [36]. Using the DF excitation, a thinner sheath together with a more pronounced ionization rate and a longer exposure time can be obtained, which could help to further improve the efficiency of plasma-assisted surface processing.
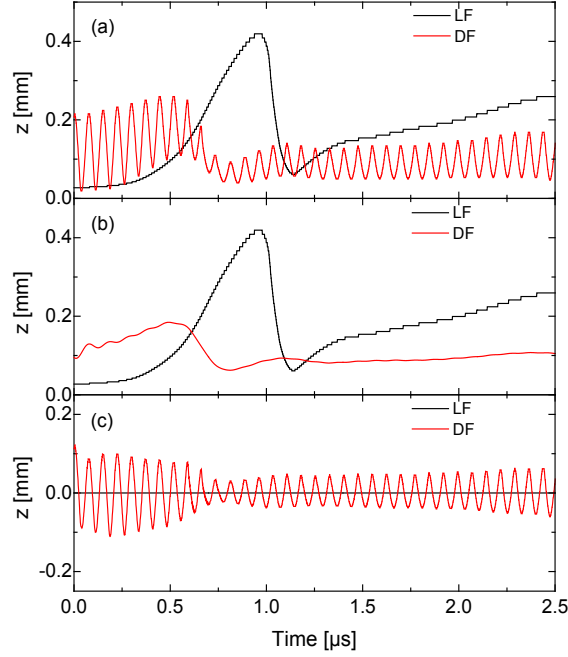
14

Figure. 12. (a) Original, (b) LF-induced and (c) RF oscillations of the sheath edge profiles near the instantaneous cathode during half LF cycle of LF (U_{LF} = 1000 V, U_{RF} = 0 V) and DF (U_{LF} = 1000 V, U_{RF} = 250 V) discharges.

3.2.2. Different phases of DF plasma

The detailed phase and space resolved plasma parameters at different phases in the initial stage of the DF discharge in Figure. 9 are presented in Figure. 13. Depending on the phase of the LF cycle, the RF oscillation results in a different discharge behaviour.

In phase (1) from 0.13 µs to 0.28 µs, the electric field is comparable on the two electrodes (Figure. 13(a)). The maximal electric field is ~1850 V/mm inside the top sheath and ~ 1780 V/mm inside the bottom sheath. The ionization only occurs within the sheath regions (Figure. 13(c)). Three structures including sheath expansion, sheath collapse and excitation within the sheath [70,73] can be observed near both the electrodes, as presented in the excitation rate profiles in Figure. 13(d) and the discharge emission in Figure. 13(e).

In phase (2) from 0.40 µs to 0.55 µs, due to the increase of the LF voltage, the sheath thickness as well as the electric field on the bottom electrode are higher than the top electrode (Figure. 13(f)). The maximal electric field is ~1550 V/mm inside the top sheath and ~ 2300 V/mm inside the bottom sheath. The ionization however can only be observed within the bottom sheath (Figure. 13(h)). The excitation rate and the discharge emission exhibit asymmetrical structure with a more pronounced discharge near the bottom electrode, see Figure. 13(i) and (j).

In phase (3) from 0.70 µs to 0.85 µs, due to the particularly high ion density close to the cathode, the sheath thickness is minimum, while the electric field is maximum close to the bottom electrode (Figure. 13(k)). The maximal electric field is ~1490 V/mm inside the top sheath and ~ 4300 V/mm inside the bottom sheath. As a result, the ionization intensity within the bottom sheath is maximum. The excitation rate and the discharge emission are pronounced in both the bottom sheath and the bulk region, as presented in Figure. 13(n) and (o).
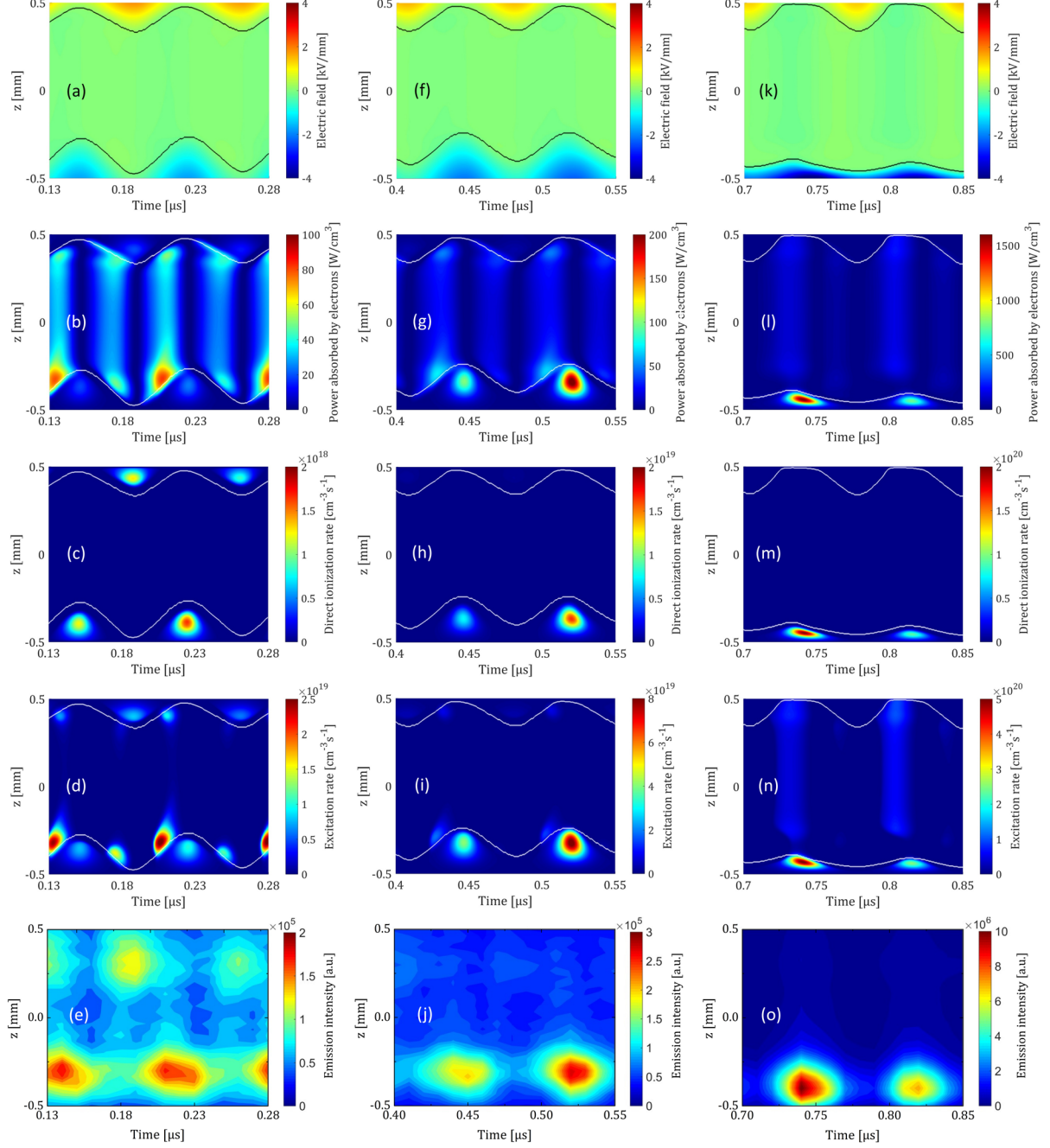
Figure. 13. Phase and space resolved electric field (first row), power absorbed by electrons (second row), direct ionization rate (third row), excitation rate (fourth row) and experimental discharge emission (fifth row) of the DF discharge with U_{LF} = 1000 V and U_{RF} = 250 V. Left column: phase (1) from 0.13 μs to 0.28 μs, middle column: phase (2) from 0.40 μs to 0.55 μs, and right column: phase (3) from 0.70 μs to 0.85 μs. The solid lines indicate the sheath edges. The numbers of the phases correspond to those in Figure. 9.

It has been demonstrated that at different phases of the LF cycle, the DF discharge experiences temporally-modulated dynamics with different ionization/excitation mechanisms depending on sheath edge, electric field and charge density. Within the sheath region, the ionization/excitation mechanisms are mainly dominated by the electric field and thus the electron energy in the sheath. The sheath expansion structure of the excitation, however, is due to the electron acceleration by the sheath oscillation towards the opposite electrode. Therefore it is mainly influenced by the sheath oscillation velocity [74] which depends on the spatial movement of the sheath edge and

thus on the local ion density [75]. When the sheath collapses, the collision rate at atmospheric-pressure is so high that the generated electrons cannot instantaneously follow the retreating sheath merely by diffusion. Instead, a self-consistent electric field builds up to drive the electrons, creating a region of negative space charge. The resulting electric field accelerates the electrons toward the electrode and heats the electrons in the process [76].

Furthermore, the time-averaged excitation/ionization rate and the EEDF profiles within the three phases in the DF discharges are shown in Figure. 14 and Figure. 15, respectively. Both the excitation and ionization rates are significantly enhanced from phase (1) to (3), and the excitation rate is approximately 10 times higher than the ionization rate. This can be explained by the different EEDF profiles of the three phases especially in the high energy tail around 11.5 eV and 15.8 eV, see Figure. 15. Therefore the DF excitation exhibits the capability of modulating electron heating in both sheath and bulk regions and thus the phase dependent EEDF [45]. This provides a further control of the plasma chemical kinetics, which can be applied to the relevant fields e.g. gas phase chemical conversion [77–81].
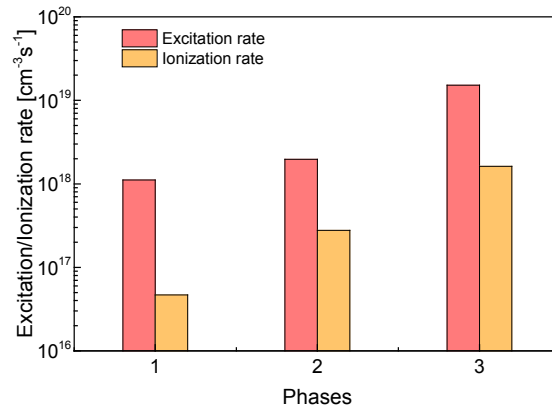

Figure. 14. Spatially integrated excitation/ionization rate within 150 ns at different phases of the DF discharge. The number of the phases correspond to those in Figure. 13.
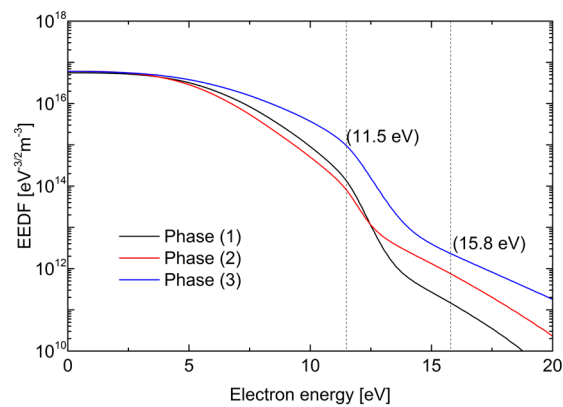

Figure. 15. Electron energy distribution function (EEDF) at different phases of the DF discharge. The number of the phases correspond to those in Figure. 13.

4. Conclusions:

A time-dependent, one-dimensional (1D) drift-diffusion model with the plasma platform PLASIMO was employed to study the atmospheric-pressure DF dielectric barrier discharges in argon. The simulation results exhibit an excellent agreement with the experimental results e.g. the electrical characteristics and the phase-resolved discharge emission. In addition, the simulation gives an insight into the DF plasma dynamics e.g. the electric field, the electron density distribution, the ionization/excitation mechanisms, the sheath edge profiles and the time dependent and averaged EEDF profiles. It is shown that the plasma conductivity is increased with the RF voltage caused by the enhancement of the plasma density. Due to the RF oscillation, the electric field and the sheath edge are temporally modulated, leading to a time-varying ionization/excitation rate. As a result, the discharge development is slowed down with a lower current amplitude and a longer duration, which can help to improve the uniformity and stability of discharge. Furthermore, with the RF voltage increasing, the averaged sheath is getting thinner with a more pronounced ionization rate and thus a higher production rate of the reactive species near the substrate, which could help to improve the efficiency of plasma-assisted surface processing. Last but not least, the DF excitation exhibits a capability of modifying the time-dependent and time-averaged EEDF, which provides a further approach to control the plasma chemical kinetics and can be applied to the other relevant fields e.g. gas phase chemical conversion.

References

[1]   U. Kogelschatz, B. Eliasson, W. Egli, *J. Phys. IV Fr.* **1997**, *07*, 47.

[2]   U. Kogelschatz, *Plasma Chem. Plasma Process.* **2003**, *23*, 1.

[3]   A. Fridman, *Plasma Chemistry*, Cambrigde University Press, New York, **2008**.

[4]   H.-E. Wagner, R. Brandenburg, K. V. Kozlov, A. Sonnenfeld, P. Michel, J. F. Behnke, *Vacuum* **2003**, *71*, 417.

[5]   N. P. Napartovich, *Plasma Polym. 6* **2001**, *6*, 1.

[6]   A. Fridman, A. Chirokov, A. Gutsol, *J. Phys. D. Appl. Phys.* **2005**, *38*, 1.

[7]   S. A. Starostin, P. A. Premkumar, M. Creatore, E. M. van Veldhuizen, H. de Vries, R. M. J. Paffen, M. C. M. van de Sanden, *Plasma Sources Sci. Technol.* **2009**, *18*, 045021.

[8]   S. Kanazawa, M. Kogoma, T. Moriwaki, S. Okazaki, *J. Phys. D. Appl. Phys.* **1988**, *21*, 838.

[9]   S. Okazaki, M. Kogoma, M. Uehara, Y. Kimura, *J. Phys. D. Appl. Phys.* **1993**, *26*, 889.

[10]   M. Kogoma, S. Okazaki, *J. Phys D Appl. Phys.* **1994**, *27*, 1985.

[11]   F. Massines, N. Gherardi, N. Naudé, P. Ségur, *Plasma Phys. Control. Fusion* **2005**, *47*, B577.

[12]   R. Brandenburg, V. A. Maiorov, Y. B. Golubovskii, H.-E. Wagner, J. Behnke, J. F. Behnke, *J. Phys. D. Appl. Phys.* **2005**, *38*, 2187.

[13]   A. V. Pipa, J. Koskulics, R. Brandenburg, T. Hoder, *Rev. Sci. Instrum.* **2012**, *83*, 115112.

[14]   P. Bruggeman, R. Brandenburg, *J. Phys. D. Appl. Phys.* **2013**, *46*, 464001.

[15]   Y. B. Golubovskii, V. A. Maiorov, J. F. Behnke, *J. Phys. D. Appl. Phys.* **2002**, *35*, 751.

[16]   Y. B. Golubovskii, V. A. Maiorov, J. Behnke, J. F. Behnke, *J. Phys. D. Appl. Phys.* **2003**, *36*, 39.

[17]   Y. B. Golubovskii, R. V. Kozakov, C. Wilke, J. Behnke, V. O. Nekutchaev, *Plasma Sources Sci.*

Technol. **2004**, *13*, 135.

[18]   Y. B. Golubovskii, V. A. Maiorov, P. Li, M. Lindmayer, *J. Phys. D. Appl. Phys.* **2006**, *39*, 1574.

[19]   V. A. Maiorov, Y. B. Golubovskii, *Plasma Sources Sci. Technol.* **2007**, *16*, S67.

[20]   Y. B. Golubovskii, R. V Kozakov, V. O. Nekuchaev, I. E. Sheykin, a Y. Skoblo, *Plasma Sources Sci. Technol.* **2010**, *19*, 045019.

[21]   S. A. Starostin, P. A. Premkumar, M. Creatore, H. De Vries, R. M. J. Paffen, M. C. M. Van De Sanden, *Appl. Phys. Lett.* **2010**, *96*, 061502.

[22]   S. A. Starostin, M. A. M. ElSabbagh, E. Aldea, H. de Vries, M. Creatore, M. C. M. van de Sanden, *IEEE Trans. Plasma Sci.* **2008**, *36*, 968.

[23]   S. A. Starostin, S. Welzel, Y. Liu, B. van der Velden-Schuermans, J. B. Bouwstra, M. C. M. van de Sanden, H. W. de Vries, *Eur. Phys. J. Appl. Phys.* **2015**, *71*, 20803.

[24]   P. A. Premkumar, S. A. Starostin, H. De Vries, M. Creatore, P. M. Koenraad, W. A. MacDonald, M. C. M. Van De Sanden, *Plasma Process. Polym.* **2012**, *9*, 1194.

[25]   P. A. Premkumar, S. A. Starostin, M. Creatore, H. De Vries, R. M. J. Paffen, P. M. Koenraad, M. C. M. Van De Sanden, *Plasma Process. Polym.* **2010**, *7*, 635.

[26]   T. Gans, D. O'Connell, V. Schulz-von der Gathen, J. Waskoenig, *Plasma Sources Sci. Technol.* **2010**, *19*, 034010.

[27]   T. Gans, V. Schulz-von Der Gathen, H. F. Döbele, *Contrib. to Plasma Phys.* **2004**, *44*, 523.

[28]   T. H. Kim, K. N. Kim, A. K. Mishra, J. S. Seo, H. B. Jeong, J. O. Bae, G. Y. Yeom, *Jpn. J. Appl. Phys.* **2013**, *52*, 9.

[29]   T. Denda, Y. Miyoshi, Y. Komukai, T. Goto, Z. L. Petrović, T. Makabe, *J. Appl. Phys.* **2004**, *95*, 870.

[30]   T. Kitajima, Y. Takeo, Z. L. Petrović, T. Makabe, *Appl. Phys. Lett.* **2000**, *77*, 489.

[31]   A. R. Gibson, A. Greb, W. G. Graham, T. Gans, *Appl. Phys. Lett.* **2015**, *106*, 054102.

[32]   B. Bruneau, T. Gans, D. O'Connell, A. Greb, E. V. Johnson, J. P. Booth, *Phys. Rev. Lett.* **2015**, *114*, 125002.

[33]   P. C. Boyle, J. Robiche, M. M. Turner, *J. Phys. D. Appl. Phys.* **2004**, *37*, 1451.

[34]   P. C. Boyle, A. R. Ellingboe, M. M. Turner, *J. Phys. D. Appl. Phys.* **2004**, *37*, 697.

[35]   N. Y. Babaeva, M. J. Kushner, *Plasma Sources Sci. Technol.* **2011**, *20*, 035017.

[36]   F. Massines, R. Bazinette, J. Paillol, in *22nd Int. Symp. Plasma Chem.*, Antwerp, Belgium, **2015**, p. O-22-3.

[37]   Z. L. Zhang, Q. Y. Nie, Z. B. Wang, X. T. Gao, F. R. Kong, Y. F. Sun, B. H. Jiang, *Phys. Plasmas* **2016**, *23*, 073501.

[38]   D. Liu, A. Yang, X. Wang, C. Chen, M. Rong, M. G. Kong, *J. Phys. D. Appl. Phys.* **2016**, *49*, 49LT01.

[39]   C. Oneill, J. Waskoenig, T. Gans, *Appl. Phys. Lett.* **2012**, *101*, 1.

[40]   A. Yang, M. Rong, X. Wang, D. Liu, M. G. Kong, *J. Phys. D. Appl. Phys.* **2013**, *46*, 415201.

[41]   Y. J. Zhou, Q. H. Yuan, F. Li, X. M. Wang, G. Q. Yin, C. Z. Dong, *Phys. Plasmas* **2013**, *20*, 113502.

[42]   D. W. Liu, J. J. Shi, M. G. Kong, *Appl. Phys. Lett.* **2007**, *90*, 2005.

[43]   K. Maeda, Y. Toda, K. Fukazawa, *EP 1 609 884 B1*, **2013**.

[44]   Y. Liu, F. J. J. Peeters, S. A. Starostin, M. C. M. Van De Sanden, H. W. De Vries, *Plasma Sources Sci. Technol.* **2018**, *27*, DOI 10.1088/1361-6595/aaa568.

[45]   Y. Liu, S. A. Starostin, F. J. J. Peeters, M. C. M. Van De Sanden, H. W. De Vries, *J. Phys. D. Appl. Phys.* **2018**, *51*, DOI 10.1088/1361-6463/aaac73.

[46]   D. B. Mihailova, Sputtering Hollow Cathode Discharges Designed for Laser Applications : Experiments and Theory, Eindhoven University of Technology, **2010**.

[47]   "https://plasimo.phys.tue.nl/," can be found under https://plasimo.phys.tue.nl/, **n.d.**

[48]   J. Van Dijk, K. Peerenboom, M. Jimenez, D. Mihailova, J. Van Der Mullen, *J. Phys. D. Appl. Phys.* **2009**, *42*, DOI 10.1088/0022-3727/42/19/194012.

[49]   M. A. Lieberman, A. J. Lichtenberg, *PRINCIPLES OF PLASMA DISCHARGES AND MATERIALS PROCESSING*, John Wiley & Sons, Inc., Hoboken, **2005**.

[50]   D. B. Mihailova, Sputtering Hollow Cathode Discharges Designed for Laser Applications, Eindhoven University of Technology, The Netherlands, **2010**.

[51]   R. Y. Pai, E. W. Mcdaniel, L. A. Viehland, *At. Data Nucl. Data Tables* **1976**.

[52]   J. F. J. Janssen, *Equilibrium and Transport in Molecular Plasmas*, **2016**.

[53]   G. J. M. Hagelaar, L. C. Pitchford, *Plasma Sources Sci. Technol.* **2005**, *14*, 722.

[54]   W. L. Morgan, "Kinema Research & Software," can be found under https://fr.lxcat.net/data/set_type.php, **2018**.

[55]   J. Gregório, P. Leprince, C. Boisse-Laporte, L. L. Alves, *Plasma Sources Sci. Technol.* **2012**, *21*, DOI 10.1088/0963-0252/21/1/015013.

[56]   A. Bogaerts, R. Gijbels, I. Introduction, *J. Appl. Phys.* **1999**, *86*, 4124.

[57]   A. Bultel, B. van Ootegem, A. Bourdon, P. Vervisch, *Phys. Rev. E - Stat. Nonlinear, Soft Matter Phys.* **2002**, *65*, 046406/1.

[58]   A. Sobota, F. Manders, E. M. Van Veldhuizen, J. Van Dijk, M. Haverlag, *IEEE Trans. Plasma Sci.* **2010**, *38*, 2289.

[59]   S. R. Sun, S. Kolev, H. X. Wang, A. Bogaerts, *Plasma Sources Sci. Technol.* **2017**, *26*, DOI 10.1088/0963-0252/26/1/015003.

[60]   S. A. Starostin, S. Welzel, M. C. M. van de Sanden, J. B. Bouwstra, H. W. de Vries, in *Proc. XXII Europhys. Conf. At. Mol. Phys. Ioniz. Gases*, Greifswald, Germany, **2014**, p. p.3-10-1.

[61]   A. Sobota, J. Van Dijk, M. Haverlag, *J. Phys. D. Appl. Phys.* **2011**, *44*, DOI 10.1088/0022-3727/44/22/224002.

[62]   R. Bazinette, R. Subileau, J. Paillol, F. Massines, *Plasma Sources Sci. Technol.* **2014**, *23*, 035008.

[63]   S. Liu, M. Neiger, *J. Phys. D. Appl. Phys.* **2001**, *34*, 1632.

[64]   F. J. J. Peeters, M. C. M. van de Sanden, *Plasma Sources Sci. Technol.* **2015**, *24*, 015016.

[65]   T. C. Manley, *J. Electrochem. Soc.* **1943**, *84*, 83.

[66]   Z. Falkenstein, J. J. Coogan, *J. Phys. D. Appl. Phys.* **1999**, *30*, 817.

[67]   S. Liu, M. Neiger, *J. Phys. D. Appl. Phys.* **2003**, *36*, 3144.

[68]   F. Massines, N. Gherardi, N. Naudé, P. Ségur, *Eur. Phys. J. Appl. Phys.* **2009**, *47*, 22805.

[69]   A. Salabaş, R. P. Brinkmann, *Japanese J. Appl. Physics, Part 1 Regul. Pap. Short Notes Rev. Pap.* **2006**, *45*, 5203.

[70]   D. W. Liu, F. Iza, M. G. Kong, *Appl. Phys. Lett.* **2008**, *93*, 1.

[71]   X. Y. Liu, J. T. Hu, J. H. Liu, Z. L. Xiong, D. W. Liu, X. P. Lu, J. J. Shi, *Appl. Phys. Lett.* **2012**, *101*, 043705.

[72]   K. Niemi, S. Reuter, L. M. Graham, J. Waskoenig, T. Gans, *Appl. Phys. Lett.* **2009**, *95*, DOI 10.1063/1.3242382.

[73]   F. Iza, J. K. Lee, M. G. Kong, *Phys. Rev. Lett.* **2007**, *99*, 2.

[74]   J. Schulze, Z. Donkó, E. Schüngel, U. Czarnetzki, *Plasma Sources Sci. Technol.* **2011**, *20*, 045007.

[75]   T. Gans, J. Schulze, D. O'Connell, U. Czarnetzki, R. Faulkner, A. R. Ellingboe, M. M. Turner, *Appl. Phys. Lett.* **2006**, *89*, 261502.

[76]   J. Waskoenig, T. Gans, *Appl. Phys. Lett.* **2010**, *96*, 181501.

[77]   I. Adamovich, S. D. Baalrud, A. Bogaerts, P. J. Bruggeman, M. Cappelli, V. Colombo, U. Czarnetzki, U. Ebert, J. G. Eden, P. Favia, D. B. Graves, S. Hamaguchi, G. Hieftje, M. Hori, I. D. Kaganovich, U.

Kortshagen, M. J. Kushner, N. J. Mason, S. Mazouffre, S. M. Thagard, H.-R. Metelmann, A. Mizuno, E. Moreau, A. B. Murphy, B. A. Niemira, G. S. Oehrlein, Z. L. Petrovic, L. C. Pitchford, Y.-K. Pu, S. Rauf, O. Sakai, S. Samukawa, S. Starikovskaia, J. Tennyson, K. Terashima, M. M. Turner, M. C. M. van de Sanden, A. Vardelle, *J. Phys. D. Appl. Phys.* **2017**, *50*, 323001.

[78]   G. J. van Rooij, D. C. M. van den Bekerom, N. den Harder, T. Minea, G. Berden, W. A. Bongers, R. Engeln, M. F. Graswinckel, E. Zoethout, M. C. M. van de Sanden, *Faraday Discuss.* **2015**, *183*, 233.

[79]   S. A. Nair, T. Nozaki, K. Okazaki, *Chem. Eng. J.* **2007**, *132*, 85.

[80]   A. Anastasopoulou, Q. Wang, V. Hessel, J. Lang, *Processes* **2014**, *2*, 694.

[81]   K. Urashima, J. S. Chang, *IEEE Trans. Dielectr. Electr. Insul.* **2000**, *7*, 602.